Supplementary Information

for

Negative differential resistance and hysteresis in graphene-based organic light-emitting devices

Qin Zhang,[a] Shufen Chen,[ab]* Shuai Zhang,[a] Wenjuan Shang,[ac] Lihui Liu,[a] Minghao Wang,[a] Hongtao Yu,[a] Lingling Deng,[a] Guangqin Qi,[a] Laiyuan Wang,[a] Sanyang Han,[a] Bo Hu,[a] Qi Kang,[a] Yuejiao Liu,[a] Mingdong Yi,[a] Yanwen Ma,[a] Wenjing Yang,[a] Jing Feng,[c] Xiaogang Liu,[de] Hongbo Sun[c] and Wei Huang[ab]*

a Key Laboratory for Organic Electronics and Information Displays & Jiangsu Key Laboratory for Biosensors, Institute of Advanced Materials (IAM), Jiangsu National Synergetic Innovation Center for Advanced Materials (SICAM), Nanjing University of Posts & Telecommunications (NUPT), 9 Wenyuan Road, Nanjing 210023, China

b Shaanxi Institute of Flexible Electronics (SIFE), Northwestern Polytechnical University (NPU), 127 West Youyi Road, Xi'an 710072, Shaanxi, China

c State Key Laboratory on Integrated Optoelectronics, College of Electronic Science and Engineering, Jilin University, Changchun 130012, China

d Department of Chemistry, National University of Singapore, Singapore 117543, Singapore

e Centre for Functional Materials, NUS (Suzhou) Research Institute, Suzhou 215123, China

* Correspondence should be addressed to e-mail: iamsfchen@njupt.edu.cn or wei-huang@njtech.edu.cn.

The AFM images of bare graphene, graphene/PEDOT:PSS with one-step and two-step coating processes were shown in Fig. S1. All graphene samples were transferred onto SiO_2/Si substrates. Obvious edges of graphene are observed in panels (a), (c) and (e) under low magnification, which correspond to bare graphene, graphene/PEDOT:PSS with one-step and two-step coating processes, respectively. Panels (b), (d) and (f) are the enlarged diagrams of panels (a), (c) and (e) in the dashed box area, respectively.

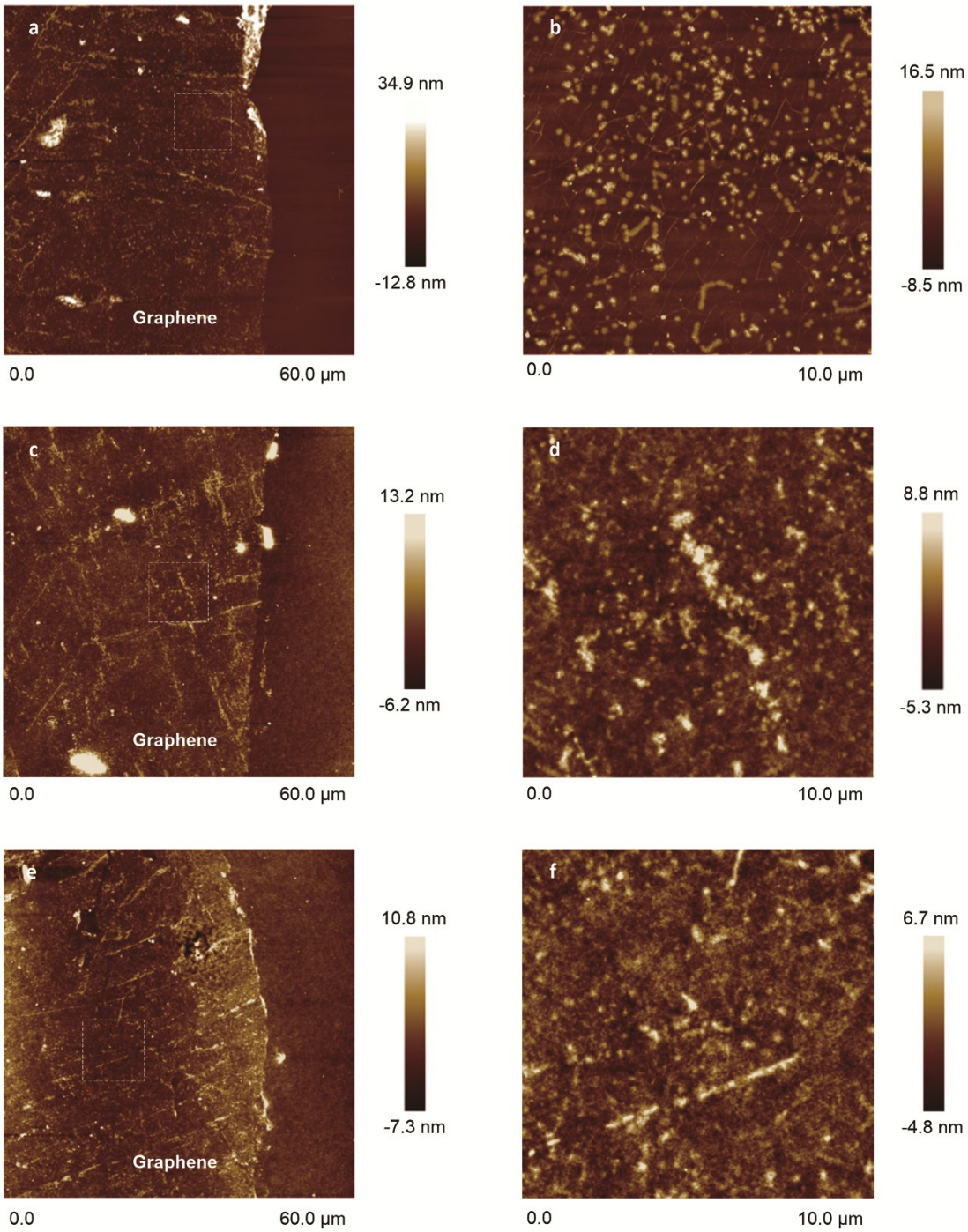

Fig. S1 AFM images of (a, b) bare graphene, graphene/PEDOT:PSS with (c, d) one-step and (e, f) two-step coating processes. Obvious edges of graphene are observed in panels (a), (c) and (e) under low magnification. Panels (b), (d) and (f) are the enlarged diagrams of panels (a), (c) and (e) in the dashed box area, respectively. The RMS for (b) the bare graphene, the graphene/PEDOT:PSS with (d) one-step and (f) two-step coating processes is 2.25, 1.28 and 1.13 nm, respectively.

Statistics on (a) D and G band peaks of TLG, (b) C_β=C_β stretch, (c) symmetric C_α=C_β (—O) stretch, and (d) C=C & ring stretch modes of PEDOT:PSS-modified TLG (with once and twice spin-coating of PEDOT:PSS) were shown in Fig. S2. About fifty different zones were measured for each structure. Here, the pure PEDOT:PSS was also measured for comparison. The C_β=C_β, symmetric C_α=C_β (—O), C=C and ring stretch modes from PEDOT:PSS will replace the D, G and 2D band peaks of TLG when coating PEDOT:PSS onto TLG, as shown in Fig. 1c-f in the manuscript. Compared to the intrinsic PEDOT:PSS, the C_β=C_β, symmetric C_α=C_β (—O), C=C and ring stretch modes redshifted when spincoating PEDOT:PSS onto TLG, indicative of the interaction between PEDOT:PSS and TLG.

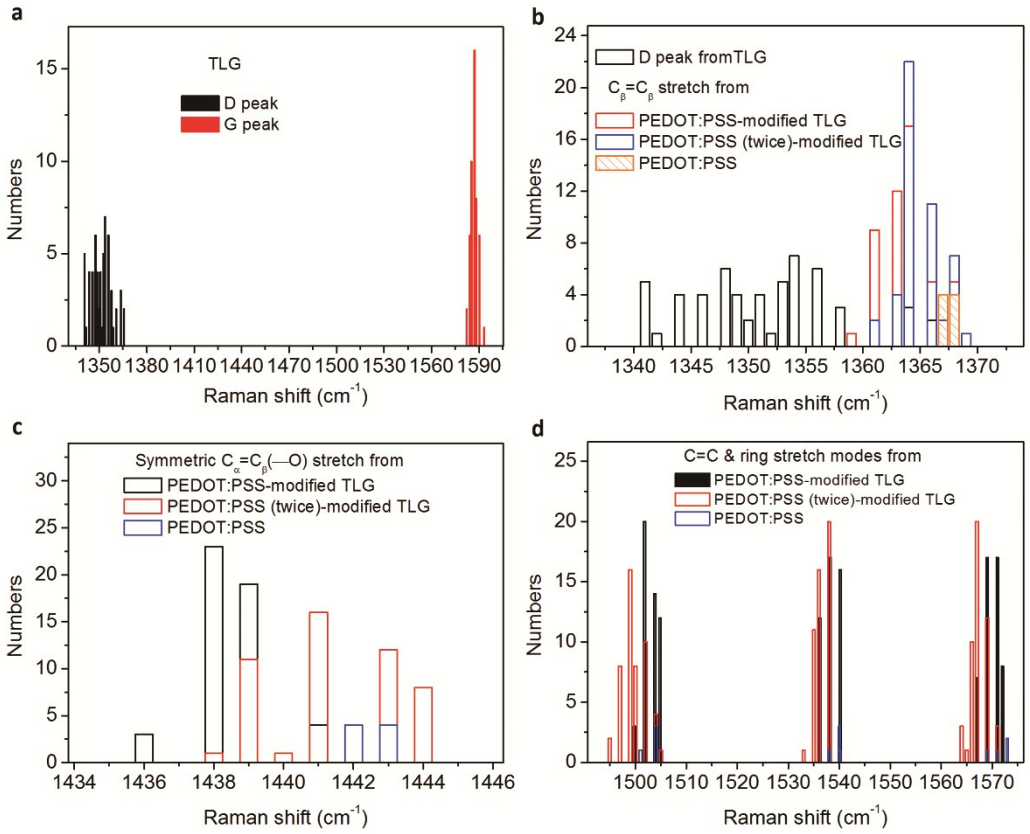

Fig. S2 Statistics on (a) D and G band peaks of TLG, (b) C_β=C_β stretch, (c) symmetric C_α=C_β (—O) stretch, and (d) C=C & ring stretch modes of PEDOT:PSS-modified TLG (with once and twice spin-coating of PEDOT:PSS).

Theory models of space-charge-limited current (SCLC) and trapped-charge-limited current (TCLC) are usually employed to systematically study the effects of temperature, organic layer thickness and mobility, and composition on current conduction and electroluminescent (EL) mechanisms of OLEDs. In this manuscript, we fitted the *J-V* characteristics of our graphene-based OLEDs with SCLC and TCLC formulae described as

$$J_{SCLC} = \frac{9}{8}\varepsilon_0\varepsilon_r\mu_0 exp(0.89\gamma\sqrt{V/d})\frac{V^2}{d^3}$$

and

$$J_{TCLC} = N_{LUMO}\mu q^{(1-m)} \times \left(\frac{\varepsilon_0\varepsilon_r m}{N_1(m+1)}\right)^m \left(\frac{2m+1}{m+1}\right)^{(m+1)} \frac{V^{(m+1)}}{d^{(2m+1)}},$$

where ε_0 is the permittivity of free space, ε_r is the dielectric constant of the organic layers which is always assumed as 3, μ_0 is the effective mobility at zero field, μ is the mobility of carriers, γ is the field enhancement factor of the mobility, $m = T_t/T = E_t/kT$, T_t is the characteristic temperature of the exponential trap distribution, E_t is the characteristic trap energy, N_{LUMO} is the density of states in the lowest unoccupied molecular orbital (LUMO) band, N_1 is the trap concentration, V is the voltage drop across the device, and d is the organic layer thickness.

The scanned *J-V* characteristics of our graphene OLEDs can be well fitted with the TCLC mechanism among a voltage range of 6.5-11 V in forward sweep direction and 11-(-3) V in backward direction, as shown in Fig. S3. The extracted parameters including μ, N_1, N_{LUMO}, ε_r and m were listed in Table S1. Our calculation results

indicated that in the low-voltage NDR region (0-±3 V), the trap concentration was far higher than that in a high-voltage region, indicating the presence of numerous defects in the PMMA and thus low film mobility. The trap concentration clearly declined after a single or more *I-V* curves scans. Both NDR and hysteresis were essentially unnoticeable after taking five consecutive scans. Taken together, these results reveal that the cyclic scan of *I-V* curves is able to not only suppress NDR by removing the PMMA residue, but also eliminate the hysteresis by filling the bulk traps of organic materials.

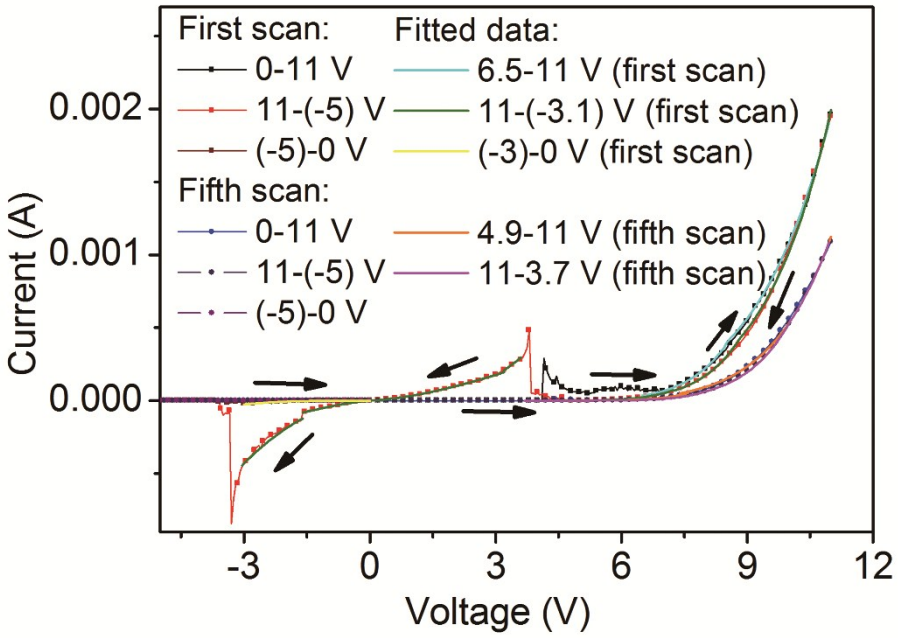

Fig. S3 Experimental and theoretical *I-V* curves of our graphene-based OLED. The theoretical *I-V* curves were fitted with a TCLC model with parameters summarized in Table S1.

Table S1 Extracted parameters from TCLC formula.

Cyclic scan Nos.	Voltage range [V]	Mobility μ [$cm^2\ V^{-1}\ S^{-1}$]	Trap concentration N_1 [cm^{-3}]	m	Scanning direction
No 1	6.5-8.3	1.4×10^{-4}	1.83×10^{17}	8	Low→High
	8.5-11	1.4×10^{-4}	2.4×10^{17}	5.2	
	11-9	1.4×10^{-4}	2.23×10^{17}	6	
	8.6-7	1.4×10^{-4}	1.85×10^{17}	8.3	
	7-4.8	1.4×10^{-4}	1.685×10^{17}	9.5	
	3.6-3.2	9.7×10^{-5}	2.3×10^{17}	2	High→Low
	3.0-1.1	3.7×10^{-5}	9.685×10^{18}	0.5	
	1.1-0	2.4×10^{-5}	5.685×10^{19}	0.35	
	0-(-1.6)	1.4×10^{-5}	6.1×10^{18}	0.35	
	(-1.65)-(-3.05)	5.4×10^{-5}	3.3×10^{17}	1	
	(-3)-(-1.1)	1.4×10^{-4}	3.3×10^{17}	2.7	Low→High
	(-1.1)-0	1.4×10^{-4}	5.3×10^{18}	1.4	
No 5	4.9-7.5	1.4×10^{-4}	1.73×10^{17}	10.5	Low→High
	7.5-11	1.4×10^{-4}	2.3×10^{17}	6.8	
	11-9.8	1.4×10^{-4}	2.3×10^{17}	6.8	
	9.8-8	1.4×10^{-4}	2.05×10^{17}	8.5	High→Low
	8.4-4.8	1.4×10^{-4}	1.77×10^{17}	10.8	
	4.8-4.4	1.4×10^{-4}	9×10^{17}	4.2	

We assumed that N_{LUMO} and ε_r are 1×10^{17} cm^{-3} and 3.

The single-hole and single-electron devices were manufactured with device structures of graphene/PEDOT:PSS (70 nm)/TAPC:26DCzPPy:PO-01 (26 nm, 4:1:0.04)/26DCzPPy:4 wt% PO-01 (15 nm)/TAPC (30 or 50 nm)/Al (100 nm) and graphene/LiF (0.5 nm)/TmPyPb (49 or 69 nm)/TAPC:26DCzPPy:PO-01 (26 nm, 4:1:0.04)/26DCzPPy:4 wt% PO-01 (15 nm)/TmPyPb (50 nm)/LiF (0.5 nm)/Al (100 nm), respectively. Note that total organic layer thickness between two electrodes in single-hole devices was equal to that in single-electron devices and two groups of devices with total organic layer thicknesses of 141 and 161 nm were respectively fabricated. Similar features were observed in single-hole devices with different organic layer thicknesses, demonstrating a universality of our results.

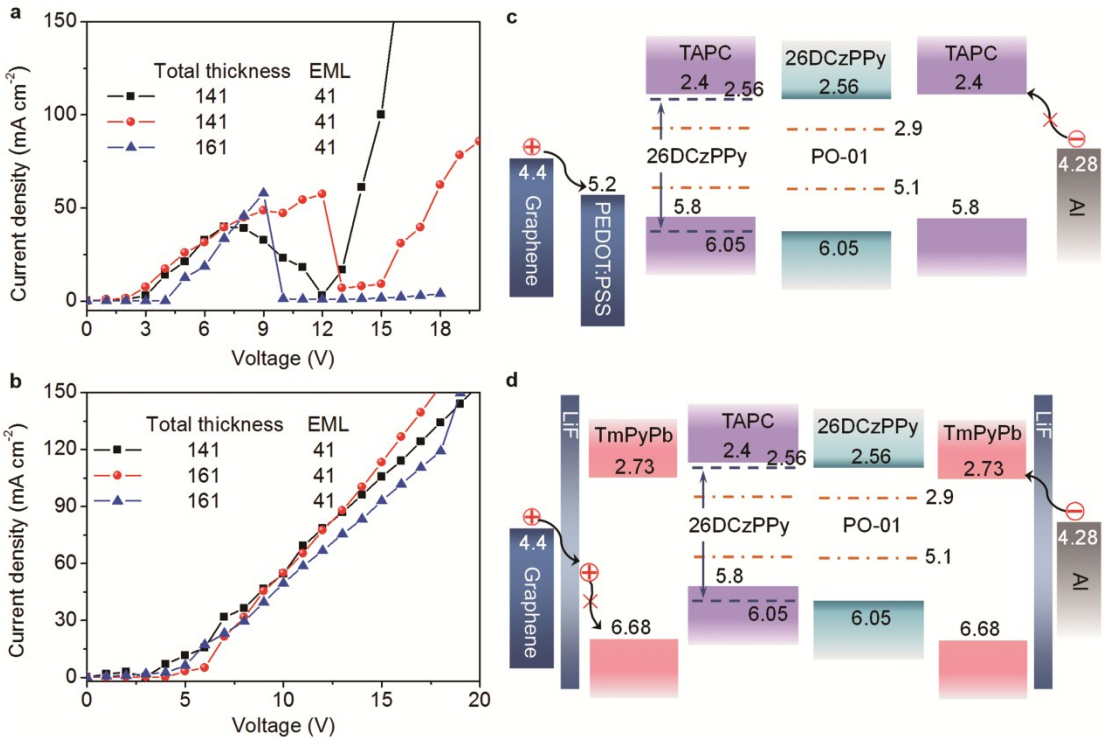

Fig. S4 *J-V* characteristics of (a) single-hole and (b) single-electron devices based on graphene anodes. Energy levels of (c) single-hole and (d) single-electron devices that respectively allow holes and electrons to inject into the devices.

Low-temperature *I-V* curves of single-hole device were measured to investigate the origin of the NDR phenomenon, with results shown in Fig. S5. The single-hole device structure is graphene/PEDOT:PSS (70 nm)/TAPC:26DCzPPy:PO-01 (26 nm, 4:1:0.04)/26DCzPPy:4 wt% PO-01 (15 nm)/TAPC (50 nm)/Al (100 nm) with a total organic layer thickness of 161 nm. The *I-V* curves were measured at 77 K in liquid nitrogen with different sweep rates of 1 and 0.07 V/s.

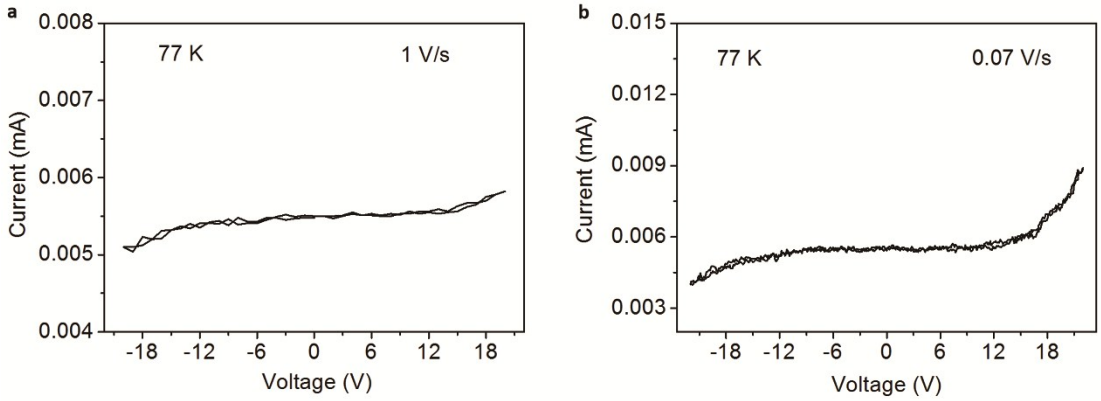

Fig. S5 Low-temperature *I-V* curves of single-hole device. The *I-V* curves were measured at 77 K in liquid nitrogen with different sweep rates of (a) 1 and (b) 0.07 V/s.

Similarly, the room-temperature *I-V* curves of single-hole device with different sweep rates were measured to observe the influence of oxygen ions migration, as shown in Fig. S6. The structure of single-hole device is same with that used in Fig. S5. Here, fast and slow sweep rates were 1 and 0.07 V/s.

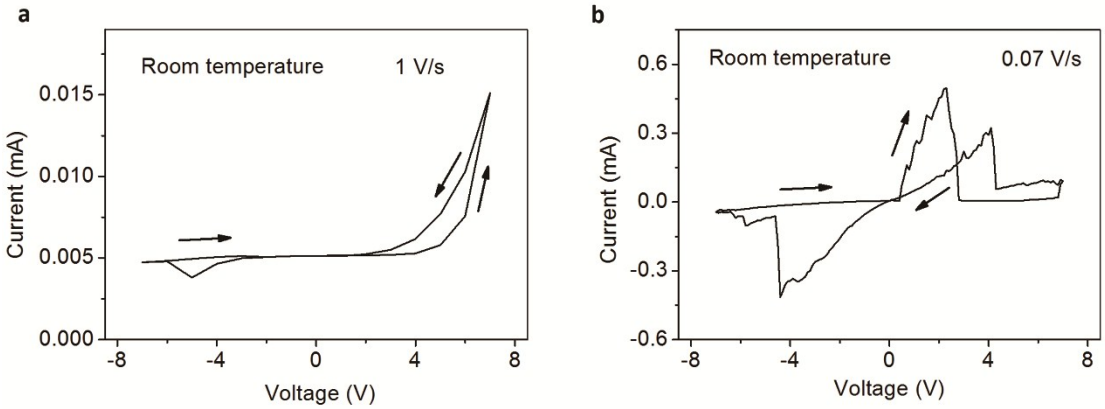

Fig. S6 Room-temperature *I-V* curves of single-hole device with different sweep rates. (a) Fast and (b) slow sweep rates of 1 and 0.07 V/s were respectively measured to observe the influence of oxygen ions migration.

Fig. S7 shows the AFM images of graphene's surface under (a) low and (b-e) high magnifications. Obvious edge of graphene is observed in panels (a) under low magnification. Panels (b), (c), d) and (e) are enlarged diagrams in the box of the panel (a). The images (b-e) were treated with a 2 mA current for 0, 2, 5 and 10 min, respectively. Pre-scanning graphene sheets with a 2 mA current for 2 min lead to a significant decomposition of PMMA and part of byproducts re-aggregated again driven by electrical Joule heating, as the top bright zone in panel (e).

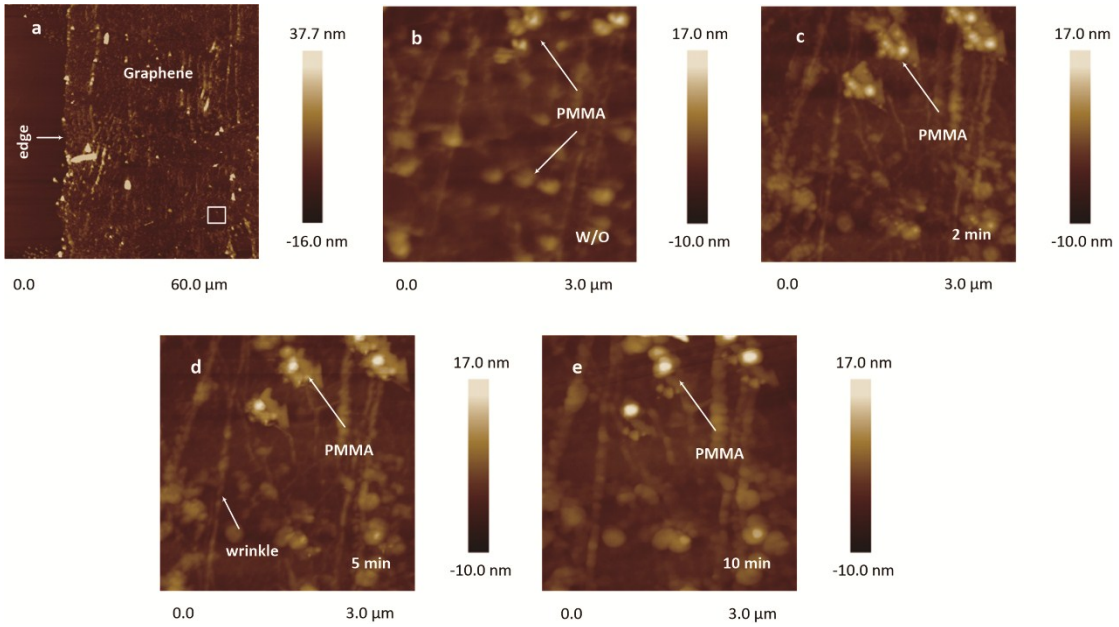

Fig. S7 AFM images of graphene's surface with current treatments for (a,b) 0 min, (c) 2 min, (d) 5 min and (e) 10 min. Obvious edge of graphene is observed in panels (a) under low magnification. Panels (b), (c), d) and (e) are enlarged diagrams in the box of the panel (a). Pre-scanning graphene sheets with a 2 mA current for 2 min lead to a significant decomposition of PMMA and part of byproducts re-aggregated again driven by electrical Joule heating, as the top bright zone in panel (e).

Fig. S8 compares X-ray photoelectron spectroscopic (XPS) characterization of our graphene electrodes without any treatment and with a high-temperature sintering process (500 °C for 4 h). From the result in Fig. S8, we were surprised to find the C—O and O—C=O bonds that represent PMMA still existed on graphene after a 4-h high temperature sintering process in a horizontal tube furnace with an Ar gas flow of 60 sccm. Compared the intensities of the C—O and O—C=O bonds in Fig. S 8 (b) with those in Fig. 5 (b) in the text, we found that the current annealing approach exhibited a similar effect as high temperature sintering method, but it is worthy noted that a current annealing has advantages of lower costs and simpler process without additional treatment equipment.

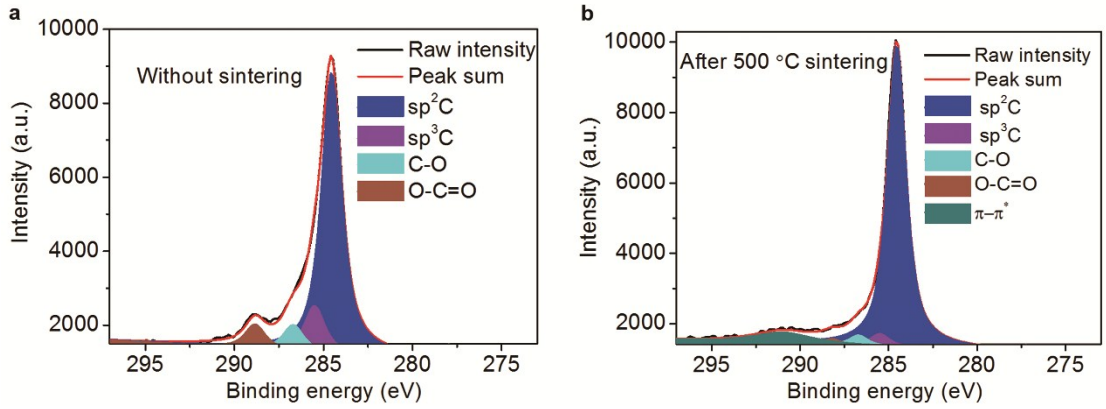

Fig. S8 XPS spectra of graphene. The C 1s spectra components (a) before and (b) after 500 °C high-temperature sintering process of TLG. The high temperature sintering process lasted for 4 hours in a horizontal tube furnace with an Ar gas flow of 60 sccm. Even if the high temperature sintering time was increased to 6 hours, the C—O and O—C=O bonds were also observed, indicating the PMMA residue is hard to be totally removed from graphene's surface.